

Description of the local series resistance of real solar cells by separate horizontal and vertical components

F. Fröhau^{a,*}, Y. Sayad^b, O. Breitenstein^a

^a Max Planck Institute of Microstructure Physics, Halle, Germany

^b University of Mohamed Chérif Messaâdia, Souk-Ahras 41000, Algeria



ARTICLE INFO

Article history:

Received 2 February 2016

Received in revised form

31 March 2016

Accepted 6 April 2016

Available online 30 April 2016

Keywords:

Lock-in thermography

Electroluminescence imaging

Photoluminescence imaging

Device simulation

Local series resistance

ABSTRACT

All previous concepts for describing the effective local series resistance of really existing solar cells, as it can be measured e.g. by luminescence imaging, try to describe it by a single local number. In solar cells showing an inhomogeneous saturation current density, this results in different series resistance images for the dark and illuminated case. The reason is the distributed character of the series resistance and the different diode current profiles under these different conditions. In this work the well-known finite element concept is used for describing a solar cell, which contains separate resistors carrying horizontal and vertical currents. A strategy is proposed how to fit these resistors to results of electroluminescence and lock-in thermography images of a real solar cell, leading to separate images of the local horizontal grid resistance, which may also show broken gridlines, and the local vertical/lumped emitter contact resistance'. The latter lumps all resistive inhomogeneities of the cell, caused by a possibly inhomogeneous contact-, emitter-, grid-, bulk-, and back contact resistance. It will be shown that this description of the local series resistance reasonably describes both the dark and illuminated case, even in inhomogeneous multicrystalline silicon solar cells.

© 2016 Elsevier B.V. All rights reserved.

1. Introduction

The series resistance is one of the basic solar cell parameters, which decisively influences its fill factor and thus its efficiency. In a solar cell different regions may contribute differently to the global series resistance of the cell. If the elementary local resistances in a solar cell are known, like the grid-, emitter-, bulk-, and contact resistances, finite element-based methods can be used to model their influence on the efficiency of the cell under operation conditions, see e.g. [1,2]. However, until now this method cannot be used for a given solar cell where the local resistance parameters are unknown and are possibly irregular. For visualizing the effective local series resistance in such devices and identifying local series resistance problems, like broken gridlines or regions with intolerable contact resistance, several series resistance imaging methods are used. The most direct method for imaging the local grid contact resistance is Corescan [3]. In this method a region of the short-circuited cell is illuminated and the local emitter voltage is measured in this region by scratching the surface with a metal wire. Unfortunately, this method is not strictly nondestructive, and it maps and displays only the local emitter voltage under this

particular illumination and loading condition and not a local series resistance.

There are several possibilities to define a local series resistance $R_s(x,y)$. Most of the present R_s imaging methods define R_s as the local voltage drop between the bias V applied at the busbars (assumed to have zero resistance, like the back contact) and the local diode voltage $V_d(x,y)$, divided by the local diode current density $J_d(x,y)$:

$$R_s(x,y) = \frac{V - V_d(x,y)}{J_d(x,y)}. \quad (1)$$

In (1) and in the following the dark diode current is defined as positive and the photocurrent as negative. This 'area-related' R_s has the unit of Ωcm^2 . This definition was used right from the beginning of solar cell research for describing the global series resistances of cells of different size, thereby ensuring that the series resistance is independent of the area A of the cell. Implicitly it was assumed there that the influence of R_s is homogeneous across the cell, and that a large cell is the parallel circuit of smaller cells. Under this condition the 'real' R_s given in the unit Ω can simply be obtained from the area-related R_s by dividing it through the cell area A . For an inhomogeneous solar cell, however, which contains e.g. regions of increased saturation current density J_{01} or regions of locally increased contact resistances, the definition in (1) is equivalent to the model of independent diodes, which is

* Corresponding author.

E-mail address: fruehauf@mpi-halle.mpg.de (F. Fröhau).

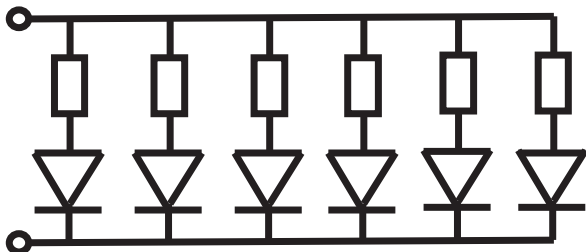


Fig. 1. Independent diode model of a solar cell.

sketched in Fig. 1. Here it is assumed that the cell consists of a parallel circuit of single diodes plus a series resistor, and that each resistor carries only the current of this connected diode. According to our knowledge, this independent diode model was used first by Mijnarends et al. [4] for considering extended macroscopic regions of different properties in a solar cell, which can indeed be assumed to be switched in parallel. Trupke et al. [5] have applied this model to each pixel of an image of a solar cell in photoluminescence (PL) imaging, and most other authors have followed this approach. It was used e.g. by Haunschild et al. [6] for interpreting electroluminescence (EL) images, by Glatthaar et al. [7,8], Kampwerth et al. [9] (in a somewhat modified form), and Shen et al. [10] for interpreting PL images, and by Ramspeck et al. [11] in their 'RESI' (REcombination current and Series resistance Imaging) method. The latter method measures the local current density by dark lock-in thermography (DLIT) and the local diode voltage by EL and leads to an R_s image after (1) for the dark case. Though PL-measured R_s and RESI- R_s are based on the same Eq. (1), both images for the same multicrystalline cell look differently [12,13]. In particular, the RESI- R_s image shows local minima in the positions of local J_{01} maxima, which are not visible in PL- R_s . The reason for this difference is meanwhile well understood [13]. It is due to the qualitatively different diode current profiles for both conditions (dark: very inhomogeneous in multicrystalline (mc) cells; illuminated under current extraction: nearly homogeneous) in combination with the too simple model of independent diodes (Fig. 1 and Eq. (1)) used for calculating R_s .

In reality we know that most part of the series resistance of a solar cell is given by the resistance of horizontal conductors, like the gridlines and the emitter layer, see e.g. [14,15]. In these conductors current contributions are flowing from many elementary diodes in different positions, not only from the position of the considered conductor. Hence these conductors represent a so-called distributed resistance. The properties of distributed resistances and in particular their influence on the global cell characteristic are well understood now [14,15]. Nevertheless, according to our knowledge there is until now only one attempt in literature by Carstensen et al. [16,17] and Wagner et al. [18] to consider the horizontal current flow in R_s imaging of a solar cell. In this approach the local series resistance is not related to the local current density but to the global cell current, therefore it is given in the unit Ω . Unfortunately, this linear response concept is made explicit only for the evaluation of measurements under illumination. Hence, at least until now, it cannot be applied in the dark case.

In this contribution we will fit the results of DLIT and EL imaging to the elements of a 2-dimensional equivalent circuit of a solar cell, which is a finite element model. The influence of photon scattering within the EL detector is corrected, which is a presupposition to measure the local diode voltages accurately [19]. Then, by assuming certain simplifications, EL and DLIT results are fitted to an equivalent model of the investigated cell. This fit leads to an image of the local saturation current density J_{01} (assuming a constant ideality factor n_1), an image of the local grid resistance,

which is assumed to be essentially homogeneous, but shows local maxima in the positions of broken gridlines, and an image of the effective lumped grid contact resistance. By comparing the EL-measured with the simulated local diode voltages, the increased grid resistance at broken gridlines and the value of the emitter sheet resistance are obtained. We call the grid contact resistance 'lumped' here because it contains all resistive inhomogeneities of the cell, except the influence of a homogeneous emitter-, grid-, bulk-, and back contact-resistance. Therefore, in certain regions, this resistance may become considerably larger than a usual grid contact resistance.

Details of the local diode voltage measurement by EL imaging will be reported in Section 2. Then Section 3 describes the equivalent circuit for the cell used in this contribution. The fitting of resistive elements of this circuit to DLIT and EL results is described in Section 4. Section 5 describes how this circuit is evaluated self-consistently for arbitrary biasing and illumination conditions. Finally in Section 6 two different solar cells are evaluated by the method described here, and the results are compared to results of Local I-V evaluation [20,21], which is based on the model of independent diodes, and some of them to results of a Griddler simulation [2] using the same local resistance data, which provides a more realistic device simulation.

2. Mapping of local diode voltages by photon scatter-corrected EL and PL imaging

The local diode voltages are measured from luminescence images by using the well-known and generally accepted exponential dependence of the luminescence signal on the local diode voltage containing the calibration factor C_i (i =position index) [5], which can be measured by evaluating a low-current EL or a low-intensity V_{oc} -PL image. For measuring the local diode voltage at V_{mpp} under illumination by PL, the net PL image is evaluated, which is the PL image measured at V_{mpp} minus that measured under short circuit condition [5].

However, it has been found recently that, for obtaining sufficiently accurate results, it is necessary to correct the luminescence images for photon scattering in the light detector. The spectral maximum of the EL or PL signal of a silicon solar cell is at about 1150 nm [1]. This is already above the spectral detection limit of the cooled Si detector cameras used for EL and PL imaging. Hence these cameras only detect the short-wavelength fraction of the emitted radiation, peaking at about 1000 nm [22]. This wavelength belongs to a mean traveling path in silicon of still 160 μm [23], which is maybe not large compared to one imaged pixel size at the cell (152 μm for a 1024 \times 1024 pixels image of a 156 \times 156 mm^2 sized cell), but large compared to the pixel size in the detector, which is typically 13 \times 13 μm^2 [24]. This means that light may scatter within the detector chip from pixel to pixel before it is finally absorbed. This light scattering effect was reported in 2012 by Walter et al. [19]. In their work the point spread function (PSF) describing the light scattering effect was directly measured by evaluating the image of a light spot. If a measured EL or PL image is spatially deconvoluted by this PSF, the 'real' EL or PL image is expected to appear. More recently Teal and Juhl [25] have pointed to the fact that a much easier measurement of the PSF over a dynamic range of many orders of magnitude is possible by evaluating a measured edge spread function (ESF), which is the image of a homogeneously radiating area with a sharp edge to a non-radiating area in the middle. In a recent work together with Teal [26] we have tested his PSF and found that it leads to slightly wrong results. Therefore we have proposed an alternative method for converting the EL-measured ESF into the PSF, which is based on an iterative deconvolution procedure [26]. This procedure includes

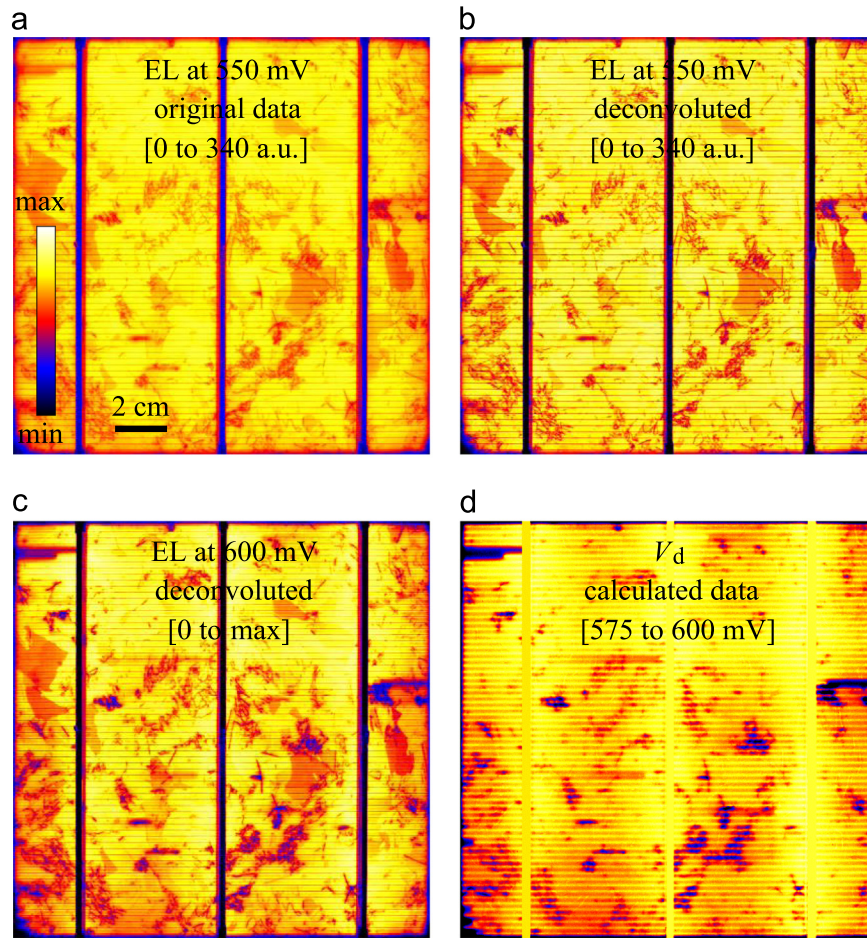


Fig. 2. EL images at low current density (a) before and (b) after deconvolution, (c) EL image at 600 mV bias after deconvolution, (d) local diode voltage calculated from (b) and (c).

a well-defined baseline shift of the data, which accounts for non-local light scattering. Note that Köntges et al. [27] have used only the subtraction of a certain percentage of the mean intensity as a heuristic method to reduce the influence of blurring effects in their luminescence investigations. Here we have used this new PSF and baseline shift method after [26] for correcting our EL and PL images for photon scatter in the detector.

Fig. 2 shows the EL image taken under low current condition at 550 mV ($< 0.1I_{sc}$) for measuring the local luminescence calibration constant [6] before (a) and after deconvolution (b), and the EL image measured at 600 mV after deconvolution (c), which was used for calculating the local diode voltage image shown in (d). We see that the deconvolution considerably increases the EL contrast. Hence, evaluating the original (not deconvoluted) images would inevitably lead to an erroneous local diode voltage distribution. The local diode voltages at 600 mV bias in Fig. 2(d), which are needed in the following as input data, are obtained here by evaluating the deconvoluted EL images in Fig. 2(b) and (c) using the 'EL-Fit' procedure [28], which is available [29]. This procedure considers local R_s influences also in the scaling measurement. The local diode current densities at 600 mV, which are the second set of input data, are obtained from DLIT measurements by using the 'Local I-V 2' evaluation procedure [20,21,29].

3. The 2-dimensional equivalent circuit

Fig. 3 shows the equivalent circuit for a silicon solar cell used in this work. While the measured DLIT images have a resolution of

512 × 512 pixels (pixel size 304 μm) and the EL images of 1024 × 1024 pixels (pixel size 152 μm), the circuit in Fig. 3 shows a pixel size of 328 × 328 μm². This leads, for the grid distance of our cell of 2.29 mm and 68 gridlines, to exactly 6 diodes between two gridlines and one diode below each gridline, as shown in Fig. 3. All primary image data were resampled to this size. This circuit is simplified compared to similar circuits used e.g. in [1,2]. Here the busbar and the back contact are assumed not to contribute to the series resistance, and the lateral conduction in the bulk is neglected. The diode resistance R_{diode} in z-direction includes the bulk and the back contact resistance. Moreover, here only the emitter resistors in main current direction are drawn (from grid to grid), in reality similar emitter resistors also exist perpendicular to these. Hence, here we assume that the current in the emitter flows essentially perpendicular to the gridlines. Since we work here with a DLIT-based low resolution diode dark current distribution, which does not contain strong gradients in x-direction, this may be a good approximation. It only will lead to errors in the regions close to the busbars or close to broken gridlines, where significant currents in x-direction are expected. The advantage of this simplified circuit is that it still can be evaluated by elementary mathematical methods, as will be shown below.

The grid resistances R_{grid} and the emitter resistances $R_{emitter}$ carry horizontal currents. Hence, these are distributed resistances [14], for which the independent diode model certainly does not hold. Only the local diode resistors R_{diode} and the lumped grid contact resistors $R_{l,contact}$ carry vertical currents through the diodes, the latter to several diodes. In our treatment the local diode resistance R_{diode} is taken homogeneously as the sum of the

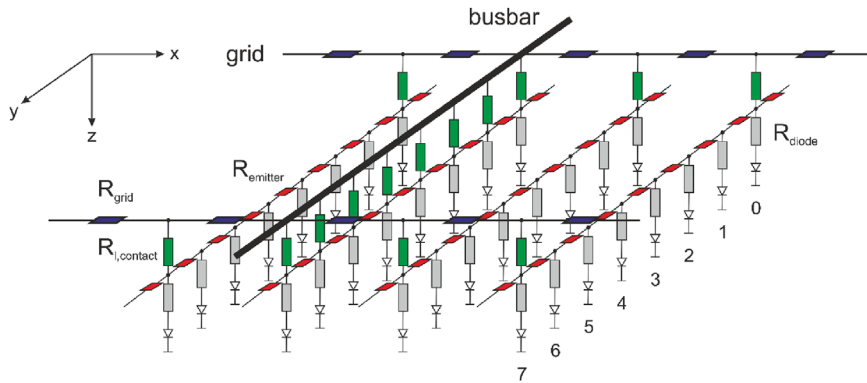


Fig. 3. Equivalent circuit of silicon solar cell used in this work. The diode indices between the gridlines are indicated.

bulk and the back contact resistances for current flow in z -direction. As mentioned in the Introduction, any inhomogeneities of R_{diode} , as well as local variations of R_{emitter} and R_{grid} (except broken gridlines) are expressed in our model by the lumped contact resistance $R_{l,\text{contact}}$. The local diodes are characterized here only by their saturation current density $J_{01}(x,y)$ and their ideality factor n_1 . The ideality factor of the first diode n_1 is taken as a parameter for considering an injection-level dependent lifetime [30,31]. For the fitting of the resistors in our equivalent circuit we anyway only use the DLIT-measured local currents at 0.6 V applied bias. Hence, this procedure is independent of the local diode model. Only for applying our model to the illuminated case (see Section 4) we need a local diode model. It would be no problem to extend our model to a 2-diode model including a parallel resistance. However, it has been shown in many DLIT analyses (e.g. in [12,20,32]) that the second diode (recombination in the depletion region) and parallel ohmic resistances are always highly localized and do not play a major role in well-processed silicon solar cells. Hence, by using a one-diode model without ohmic shunts we expect wrongly predicted local diode voltage data only in the few positions of J_{02} -type and ohmic shunts.

Since we have only two images for evaluation available, which are the local diode voltage resulting from an EL image and the local dark current density from a DLIT image, both taken at the same bias of typically 600 mV, we can fit only two free parameters per pixel. These are J_{01} of the diodes and the lumped grid contact resistances $R_{l,\text{contact}}$. All other resistances in Fig. 3 have to be assumed as known, first. However, from evaluating the local diode voltage distribution we obtain information on the value of the homogeneously assumed emitter sheet resistances R_{emitter} , and we may distinguish between broken gridlines, which only influence the region below one gridline, and regions of locally increased contact resistance. Moreover, from evaluating the $R_{l,\text{contact}}$ distribution, we obtain additional information to the homogeneous value of R_{grid} and to its value in the position of broken gridlines.

The saturation current density J_{01} of the diodes can be obtained directly from the input data $V_d(x,y)$ and $J_d(x,y)$:

$$J_{01}(x,y) = J_d(x,y) \exp\left(-\frac{V_d(x,y)}{n_1 V_T}\right). \quad (2)$$

Here V_T is the thermal voltage (25.69 mV at 25 °C). This method was used already in the RESI concept [11]. Note that here we cannot use the local diode voltage as it comes out of the EL evaluation directly, since the DLIT-based local current density has a much lower effective spatial resolution than the EL-based local voltage. If we would calculate J_{01} from the high resolution V_d and the low resolution J_d images after (2), the result would show a J_{01} modulation between the gridlines, caused by the V_d profile there, which is unrealistic. Therefore in this work we first deconvolute the EL image for photon scatter, thermally blur it, and then

calculate V_d from this image. We have found that this procedure is equivalent to thermally blur the V_d image obtained from the scatter-deconvoluted EL images. Our procedure shows less artifacts in the busbar regions, where the luminescence signal is shadowed. Both the convolution and the deconvolution were performed by using the DECONV software, which was originally developed for evaluating DLIT images [29,33]. Note that the PSF for light scattering in the detector has a spatial extension in the order of the image size, whereas that for thermal blurring has an extension in the order of 1 cm², and both have a completely different shape. Hence the effect of the thermal convolution is by far not compensated by the effect of light scattering deconvolution.

Circuits like that in Fig. 3 are usually evaluated by SPICE methods [1]. However, our particular circuit consists only of linear lines, first the lines of the emitter resistors from gridline to gridline in y -direction, and then the lines of the grid resistors from busbar to busbar or from the edge to a busbar in x -direction. This considerably simplifies the evaluation. If we know the local diode currents and voltages from DLIT and EL measurements, we may evaluate the circuit for this particular case in an elementary way, without using any iterative methods. In the following section the details of this elementary circuit evaluation will be given. However, due to inevitable inaccuracies of the measured data, this evaluation does not deliver reliable information in broken gridline regions. This information can be gained by a fully self-consistent evaluation of the circuit, which requires an iterative method and will be outlined in Section 5. This self-consistent evaluation also allows to consider arbitrary conditions, e.g. under illumination and current extraction at the maximum power point (mpp) of the cell.

4. Elementary circuit evaluation

4.1. Treatment of diode rows attached to gridlines

In the following we consider the currents and resistors of the circuit in Fig. 3 (in units of A and Ω). Hence, knowing the size of our elementary diodes ($328 \times 328 \mu\text{m}^2$), the sheet and line resistances and current densities have to be converted correspondingly. The trick for the circuit calculation is to consider all diode currents (which we know in the measured dark case from DLIT) as constant currents. In the following, horizontal currents flowing from left to right (i.e. in x -direction in Fig. 3) and from top to bottom of the cell (i.e. in y -direction in Fig. 3) are counted positive and in the opposite direction negative. Also the indices are counted from left to right and from top to bottom. The simplest evaluation case is a vertical line of diodes coupled by emitter resistors, which is not terminated by two gridlines, as in Fig. 3, but only by one gridline on one side, here assumed to lie at the top. Hence we assume that

this line of diodes is lying at the lower edge of the cell below the last gridline. Since the dark current direction in the emitter is from top to bottom here, this current is positive. The length of this line is only half of the emitter lines shown in Fig. 3, hence we assume to have $N=3$ diodes, N emitter resistors R_{emitter} , and one lumped contact resistor $R_{\text{l,contact}}$ connecting this row to the grid. Index $n=0$ describes the diode below the gridline, $n=1$ is the uppermost diode next to the gridline, and $n=N=3$ is the lowermost diode at the lower edge of the cell.

Unfortunately, our EL measurement delivers only accurate results for the diodes between the gridlines, but not for that below the gridlines, since these are at least partly shadowed. This does not hold for the DLIT-based diode current data, since we work with local emissivity correction, hence also the DLIT data below the gridlines are reliable. Therefore we extrapolate the EL-based diode voltages below the gridlines from the known diode voltages of the three next lying non-shadowed diodes in the row by assuming a parabolic behavior. Since all gridlines are lying between two diode lines, the average value of the extrapolated voltages from the neighboring diodes from the top and from the bottom of each gridline is used. Only these extrapolated values of V_d below the gridlines are used in our method for fitting the circuit parameters, but the values of the local diode currents for all pixels are evaluated. It will be shown below that the EL-measured V_d data in the positions between the gridlines are used later on to estimate the value of the emitter resistivity and to identify positions of broken gridlines. Note that the lumped contact resistances and later on also the grid resistances are defined only in the positions of the gridlines. Therefore, the pixels in these images in the Results Section 5 will consist of horizontal stripes across the gridline positions, 7 diode positions wide. The busbar regions are not treated in our method. For them the local diode voltages are taken as that of the nearby lying diodes, the same is performed in the 'Local I-V' analysis for the local dark current densities.

From the extrapolated values of V_d below the gridlines we may calculate the emitter voltage in the pixels below the gridline, here assumed to have the position index 0:

$$V_{\text{emitter},0} = V_{d,0} + I_{d,0}R_{\text{diode}}. \quad (3)$$

This is done for all gridline positions, but this formula also holds for all pixels between gridlines. Until now we still consider only the lower edge of the cell, which is contacted to one gridline at the top. We may now calculate the local emitter currents $I_{\text{emitter},n}$. Since this current is zero at the lower edge of the cell, the horizontal emitter currents I_{emitter} in each line is the sum of all the diode currents I_d counted from the edge (here $n=N=3$) to the diode position:

$$I_{\text{emitter},n} = \sum_{i=N}^n I_{d,i}. \quad (4)$$

The current fed to the grid from this diode row is $I_{\text{emitter},1}$. The voltage drops ΔV_n across the emitter resistors R_{emitter} are:

$$\Delta V_n = I_{\text{emitter},n}R_{\text{emitter}}. \quad (5)$$

Here R_{emitter} is assumed to have a certain realistic value of e.g. $50 \Omega/\text{sq}$, which will be optimized (fitted) later on. Now we may predict the emitter voltages in all positions of this line:

$$V_{\text{emitter},n} = V_{\text{emitter},0} - \sum_{i=1}^n \Delta V_i. \quad (6)$$

The diode rows at the upper edge of the cell, above the uppermost gridline, are treated similar to the rows below the lowermost gridline, with some differences. Here all emitter currents are negative, since they point upwards. Therefore here in Eqs. (4) and (5) a minus sign has to be inserted to get positive voltage drops, and the indices in the sum in (4) are running from top to bottom ($i=1$ to n). In the sum of (6) the indices are running

here from bottom to top ($i=N=3$ to n). Note that here the emitter resistor below (in the case of grid resistors right of, see below) each diode position belong to this diode, whereas in all other cases the resistors above (resp. left of) each diode belong to this diode.

This procedure becomes only somewhat more complicated for the diode lines which are connected at both sides to two gridlines, which is the usual case. In this case $N=6$ holds, see Fig. 3. As described above, we know the diode voltages below the gridlines ($n=0$ and 7; the last diode with $n=7$ belongs already to the next gridline, see the diode indices given in Fig. 2) from interpolating the values outside of the gridlines. Then, since we know the emitter voltages at both edges of the line from (3), we calculate the potential difference between the top and the bottom end of each diode row, both diodes lying below a gridline:

$$\Delta V_{\text{emitter}} = V_{\text{emitter},0} - V_{\text{emitter},7}. \quad (7)$$

In a region of homogeneous diode current this difference would be zero. Now we again make use of the trick to assume all diode currents as constant currents, independent of the potentials. We now evaluate the diode line in two steps. In the first preliminary step we evaluate it by assuming that one of the edges (here the lower edge) would be electrically open, as in the case described above. Then we can use the same formulas (4)–(6) for evaluating this line. The results are the preliminary emitter voltages after (6), leading to the preliminary voltage drop between diodes 0 and $N=6$:

$$\Delta V_{\text{emitter}}^{\text{prelim}} = V_{\text{emitter},0} - V_{\text{emitter},6}. \quad (8)$$

Now we add a correction current I_{corr} to the whole emitter line, which ensures that the voltage drop across this line equals the real $\Delta V_{\text{emitter}}$ of (7), which we know from our measurements. This correction current does not influence the local diode currents, which are assumed to be constant currents. Here we have to consider our assumption that the emitter resistor belonging to each diode connects it to the next upper diode, but not to the next lower one. Then in our case the lowermost diode ($n=6$) must be connected to the lower gridline by an additional resistor $R_{\text{emitter},7}$, which also has to be regarded for the voltage drop of the correction current. Also in Fig. 3 there are 7 resistors between two gridlines. In (8) this resistor has not to be regarded, since in this preliminary case the current across it is zero (only the diodes between the gridlines contribute to the grid current). Finally, the correction current I_{corr} is calculated for each emitter row from solving:

$$\Delta V_{\text{emitter}} = \Delta V_{\text{emitter}}^{\text{prelim}} - 7R_{\text{emitter}}I_{\text{corr}}. \quad (9)$$

Now all preliminary horizontal emitter currents, which were calculated after (4), are corrected by this I_{corr} :

$$I_{\text{emitter},n} = I_{\text{emitter},n}^{\text{prelim}} - I_{\text{corr}}. \quad (10)$$

This allows us to calculate the final local emitter voltages by applying Eq. (6) with (5) by using (10). The current fed from the upper gridline to the uppermost diode of the line ($n=1$), which will be called later on I_{bottom} , since it comes from the bottom to the gridline, is $I_{\text{emitter},1}$ in (10). The current fed from the lower gridline ($n=7$) to the lowermost diode ($n=6$) (this current will later be called I_{top}) is $-I_{\text{corr}}$ from (9). The minus sign means here that this dark current is flowing from bottom to top.

If all diode rows between the gridlines and at the edges are treated as described above, for all pixels outside of the busbars simulated local emitter voltage data after (6) and (3) are calculated. These data only use the EL-based (extrapolated) local diode voltages below the gridlines and the current data of all positions. The calculated values consider the voltage drops due to the real lateral currents in the emitter layer. Therefore these data can be

used now to obtain information on the emitter conductivity. From the local emitter voltages the simulated local diode voltages can be obtained by correcting the voltage drops at R_{diode} after (3). A comparison of these simulated local diode voltages with the EL-measured V_d image, namely evaluating the parabolic drop between the gridlines, gives us information how correctly the emitter sheet resistance was assumed. This sheet resistance is then varied until a reasonable agreement between simulated and EL-measured local diode voltage data is obtained in regions without broken gridlines. In particular for this procedure we urgently need the photon scatter correction of the EL images after Section 2. We have found that, if the raw EL images are used for this evaluation, a too low emitter sheet resistance is obtained here.

4.2. Treatment of the grid

Before we can calculate $R_{\text{l, contact}}$ we need to calculate the local grid voltages from the currents fed to the grid. Knowing $V_{\text{emitter},0}$ below the gridline from (3) and the emitter currents fed into the gridlines from (9) and (10) resp. (4) for the rows lying at the cell edge, we may calculate now the lumped contact resistances $R_{\text{l, contact}}$ between the emitter and the grid in these positions. Here we have to regard that each pixel below a gridline is fed by two rows of diodes, one at the bottom and another one at the top. Then the total current flowing through $R_{\text{l, contact}}$ is the sum of that coming from the bottom diode row I_{bottom} , plus the diode current of the diode below the grid $I_{\text{d,0}}$, plus the current coming from the top row of diodes I_{top} , see the discussion of (9) and (10).

$$I_{\text{Rcontact}} = I_{\text{bottom}} + I_{\text{d,0}} - I_{\text{top}} \quad (11)$$

The minus sign before I_{top} is due to the fact that this current is counted here negative because it flows from bottom to top, nevertheless it adds to the current through $R_{\text{l, contact}}$. The next task is to calculate the local grid voltages. At the beginning we assume that all grid resistances R_{grid} would be the same, and we assume a reasonable value for them. Again, we have to distinguish between gridlines at the edge of the cell, connected to only one busbar, and gridlines between two busbars, where we have to use the two-step method with the correction current. The principle of the treatment is exactly the same as for the rows of diodes between two gridlines. Then I_{emitter} becomes I_{grid} , we have to replace the diode currents I_{d} by the currents through $R_{\text{l, contact}}$ of (11), the emitter voltages in gridline position by the applied busbar bias V (here assumed to be the same for all busbars, hence ΔV according to (9) is zero), R_{emitter} is replaced by R_{grid} and N by the number of grid resistances in each gridline N_{grid} . Later on we will consider the influence of broken gridlines, see next section. For gridlines connected to only one busbar the calculations are performed in analogy to (4)–(6), and for a gridline lying between two busbars (5) and (9) must be replaced by:

$$\Delta V_n = I_{\text{grid},n} R_{\text{grid},n} \quad (12)$$

$$0 = \Delta V_{\text{grid}}^{\text{prelim}} - \sum_{i=1}^{N_{\text{grid}}+1} R_{\text{grid},i} I_{\text{corr}}. \quad (13)$$

From (13) for each gridline again a correction current I_{corr} is calculated, which is then used to correct $I_{\text{grid},n}$ in (12), leading to the local grid voltages:

$$V_{\text{grid},n} = V - \sum_{i=1}^n \Delta V_i. \quad (14)$$

For $R_{\text{grid}, N_{\text{grid}}+1}$ the assumed homogeneous value of R_{grid} is used. Now we may calculate the unknown value of $R_{\text{l, contact}}$ for all grid positions:

$$R_{\text{l, contact}} = \frac{V_{\text{grid}} - V_{\text{d,0}} - I_{\text{d,0}} R_{\text{d}}}{I_{\text{Rcontact}}}. \quad (15)$$

The image of these contact resistances is now used to optimize R_{grid} , which can be done only in regions without broken gridlines showing J_{01} as homogeneous as possible. If $R_{\text{grid}}=0$ would be assumed, the whole resistive influence of the gridlines would be attributed to $R_{\text{l, contact}}$. Then $R_{\text{l, contact}}$ would show a parabolic shape with a maximum in the middle between two busbars, as we know it from conventional effective series resistance images. If R_{grid} would be assumed too high, $R_{\text{l, contact}}$ would show a minimum between two busbars and eventually becomes negative there. Thus, R_{grid} has to be optimized until, in a homogeneous region of the cell without broken gridlines, the image of $R_{\text{l, contact}}$ looks as homogeneous as possible between two busbars.

4.3. Treatment of broken gridlines

Until now we have assumed an ideal grid without any broken gridlines. In regions of broken gridlines the local grid resistance has to be increased. The first task is to identify broken gridlines and to distinguish them from regions of increased contact resistance. This can be done by evaluating the EL-measured image of V_d and the $R_{\text{l, contact}}$ image obtained in (15) in the previous section. If a gridline should be broken exactly between two busbars, where the horizontal grid current is zero, it remains invisible and also has no impact on the cell performance. Any other broken gridline can be identified already in the EL-based V_d image as a minimum of V_d in the stripe below this gridline with a sharp onset in the position of breakage. A region of insufficient grid contact would not show such a stripe shape, it would appear spatially extended. If the cell is evaluated according to Sections 4.1 and 4.2, the position of such a broken gridline between two busbars shows up in $R_{\text{l, contact}}$ as bright lines with a dark-bright contrast in this position. This will be demonstrated in Section 6.2. Then the grid resistance $R_{\text{grid},i}$ in the breakage position has to be increased in (13) until, in the following evaluation, $R_{\text{l, contact}}$ appears homogeneous in the region of the affected gridline, hence it shows values close to the neighboring regions. Until now this local increase of $R_{\text{grid},i}$ is performed manually by 'trial and error'.

If a gridline is broken in a region outside of the busbars towards an edge, the separated fraction of the gridline is nearly isolated from the busbar, hence it does conduct only little or no current to it. This region is still electrically connected to the neighboring gridlines by the emitter resistors. Then this separated gridline fraction is expected to receive negligible net current after (11) from the diodes below. Indeed, the I_{Rcontact} image shown in the Results Section 6.1 displays values close to zero in the marked isolated grid regions. However, due to inevitable inaccuracies of our measurement and evaluation, this residual current is not exactly zero but may be weakly positive or negative. In the calculation of (15) a continuous grid is still assumed, hence there is a considerable voltage drop assumed across $R_{\text{l, contact}}$. Since the local contact currents are very low in this region, this calculation leads to very large positive or negative values of $R_{\text{l, contact}}$, depending on whether positive or negative residual values of I_{Rcontact} are present. These largely outrunning values of $R_{\text{l, contact}}$ in a line are physically meaningless, since they are due to our measurement inaccuracy and the assumption of a still intact grid. However, they may also be used to identify isolated grid regions. In the self-consistent evaluation of the equivalent circuit described in the following Section, the outrunning values of $R_{\text{l, contact}}$ in the isolated grid regions are replaced by the average values of the surrounding. In this evaluation the values of R_{grid} at the junction to isolated grid regions are optimized to lead, for the dark case at 600 mV bias, to local diode voltages fitting the EL-measured values as good as possible.

5. Self-consistent circuit evaluation

Until now we have considered the circuit in Fig. 3 only under an applied bias of typically 600 mV in the dark, where we have made EL and DLIT measurements, we have assumed that we know all local diode voltages and currents, and have asked for the values of the local resistive components of this circuit. For verifying the accuracy of our model, now we have to use these components for simulating the circuit at other biases, also under illumination and current extraction. This will be done first in the dark at 600 mV bias under the EL+DLIT measurement condition for finding the correct values of $R_{\text{grid},i}$ in all positions of broken gridlines. Then this will be done at a bias of V_{mpp} , which for our cell used in Section 6.1 is 518 mV, which is the most interesting case. In Section 6.1 we will compare the simulated local diode voltage results with that measured by PL imaging under the same conditions. We also will compare them to local diode results obtained from a Griddler [2] and from a Local I-V evaluation [20,21].

We use an iterative method for calculating the local emitter voltage data $V_{\text{emitter},i}$. The strategy is the following: In first approximation we assume certain starting values for the local emitter voltages V_{emitter} . Knowing the local values of I_{01} , R_{diode} , and I_{sc} (see below) we may calculate the local diode current I_d for all positions. From these currents, by using the method described above, we model our cell including all local emitter and grid currents and voltage drops, leading to a simulated image of V_{emitter} at the considered bias V . At the beginning these simulated values will not coincide with the assumed starting values. Now V_{emitter} is corrected by using the local differences between assumed and simulated values until the assumed values coincide with that of the simulation, leading to a self-consistent description of the illuminated cell.

In first approximation ($m=1$) we assume that V_{emitter} homogeneously equals the applied bias V :

$$V_{\text{emitter}}^{(1)} = V. \quad (16)$$

Knowing the local J_{01} data from (2), we calculate the local J_{sc} data for the illuminated case by using the empirical method introduced recently [34]. From this we calculate the expected local diode currents in this iteration:

$$I_d^{(m)} = I_{01} \exp \left[\frac{V_{\text{emitter}}^{(m)} - I_d^{(m)} R_d}{n_1 V_T} \right] - I_{\text{sc}}. \quad (17)$$

This equation is resolved to $I_d^{(m)}$ by using the Lambert W-function in Matlab [35]. Now, by using the local currents of (17) instead of the DLIT-based currents, we perform the whole procedure of Eqs. (3)–(14) for simulating the local emitter currents after (4), the emitter voltage differences to the next gridline after (6), the grid contact currents after (11), and the local grid voltages after (14).

Here the following problem occurs: In Section 4 the emitter voltages below the gridlines were known from EL results, but now they are unknown. These emitter voltages influence the currents through the contact resistors after (11). Therefore here the calculation of the local emitter voltages after (6) is performed twice, first by assuming in (7) for the emitter voltages below the gridlines the values of $V_{\text{emitter}}^{(m)}$ used in this iteration, leading to the currents fed into the gridlines after (10). Then the local grid currents are calculated by summing up these currents in each gridline, leading to the local grid voltages after (14). From them and (10) the local emitter voltages below the gridlines are corrected after:

$$V_{\text{emitter},0}^{(m,\text{corr})} = V_{\text{grid}}^{(m)} - I_{\text{Contact}}^{(m)} R_{\text{l,contact}}. \quad (18)$$

Using these corrected emitter voltages below all gridlines, now $\Delta V_{\text{emitter}}$ is re-calculated after (7), still using the currents of (17),

leading to a new correction current after (9) and finally after (6) to the simulated emitter voltages $V_{\text{emitter}}^{(m), \text{sim}}$ in this iteration. As mentioned, these simulated emitter voltages will, at the beginning of the iteration, deviate from the assumed local emitter voltages $V_{\text{emitter}}^{(m)}$. The difference is:

$$\Delta V_{\text{emitter}}^{(m)} = V_{\text{emitter}}^{(m), \text{sim}} - V_{\text{emitter}}^{(m)}. \quad (19)$$

This difference is used now to correct $V_{\text{emitter}}^{(m)}$, leading to the next iteration ($m+1$) of V_{emitter} :

$$V_{\text{emitter}}^{(m+1)} = V_{\text{emitter}}^{(m)} + S_1 \Delta V_{\text{emitter}}^{(m)} + S_2 (\Delta V_{\text{emitter}}^{(m)} - \Delta V_{\text{emitter}}^{(m-1)}). \quad (20)$$

The last term in (20) is a differential term in the feedback loop, which reduces the tendency of oscillation of the result. S_1 and S_2 are slope factors, which determine the speed of the convergence. If S_1 is chosen too high, the result will oscillate from iteration to iteration, which may be prevented by increasing S_2 , and if S_1 is chosen too low the procedure will converge only slowly. It turns out that the optimum values of S depend on the position in the cell. In the regular regions $S_1=S_2=0.1$ works well, but in regions of isolated gridlines S_1 must be very small to avoid oscillations.

The result of (20) is used again in (17) and this loop is repeated until convergence ($\Delta V_{\text{emitter}}=0$). The resulting V_{emitter} data are, by using the I_d data of (17), converted to V_d data after (3), which may be compared to EL- or PL-measured V_d data or data simulated by alternative methods, see Section 6. The comparison with EL-measured V_d data allows to optimize $R_{\text{grid},i}$ realistically also in that positions of broken gridlines, which lead to isolated gridline regions.

6. Results

6.1. Cell with broken gridlines

The method described in this contribution was first applied to an industrial multicrystalline silicon cell of BSF type (1 Ωcm B-doped bulk, 190 μm thickness, about 50 Ω/sq P-doped emitter, full-area Al back contact). Fig. 4(a) shows the EL-based local diode voltage data of this cell at a bias of 600 mV in the dimensions used for our evaluation (pixel size 328 × 328 μm²), where in the gridline positions already the V_d values extrapolated from the free area data are inserted. Therefore here in the grid positions the diode voltages are slightly higher than in Fig. 2(d). In Fig. 4(a), for the diode voltages in the positions of the busbars, the data coming from the EL analysis were used, which are based on scattered light coming from the surrounding. Therefore here the local voltage data in the busbar regions are displayed slightly too low. Already this image shows regions below broken gridlines as dark stripes. Fig. 4(b) shows the local diode voltages simulated by the elementary evaluation after (6) with (3), hence based on the extrapolated local diode values below the gridlines and the lateral current flow in the emitter, assuming an emitter resistance of 40 Ω/sq. This image correlates well with image (a), hence this assumed R_{emitter} appears to be realistic. It is still somewhat smaller than the usual 50 Ω/sq, possible reasons for this will be discussed in Section 7. Fig. 4(c) shows the J_{01} image obtained from (a) and the DLIT-based J_d image after (2). Fig. 4(d) shows the RESI- R_s image after (1), which also shows the broken gridline regions as stripes of increased effective R_s and the expected local R_s minima in the positions of J_{01} maxima, see [13]. In particular, this image shows the global maximum between the busbars and also between the gridlines, as all previous R_s images did. Fig. 4(e) shows the local net current through the contact resistances below the gridlines after (11), which shows minimum values in the regions of isolated gridlines, e.g. at the top left. The original $R_{\text{l, contact}}$ data calculated

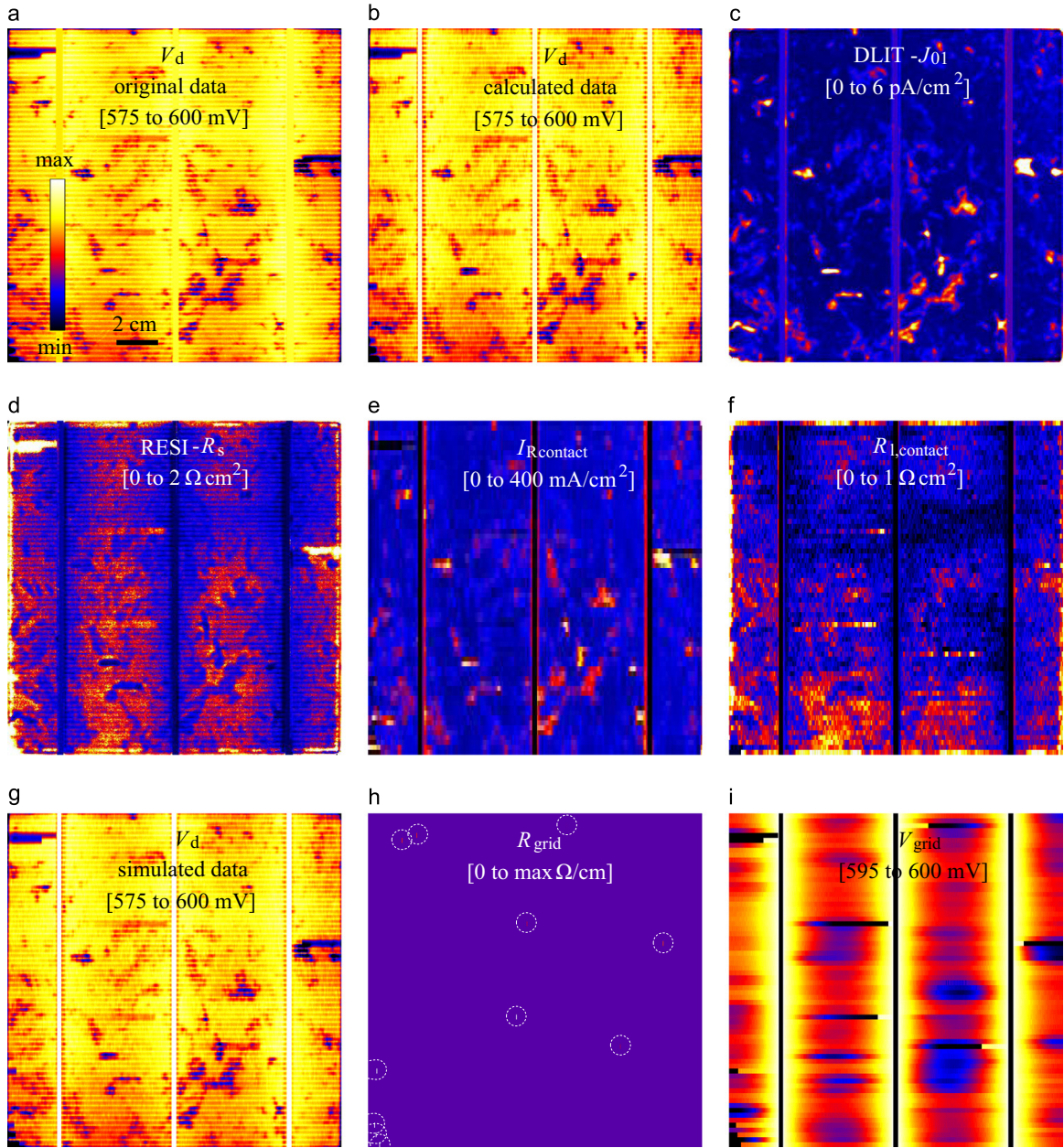


Fig. 4. (a) EL-measured V_d ; data in grid positions extrapolated, (b) V_d calculated by elementary evaluation, (c) effective J_{01} after (2), (d) RESI- R_s , (e) grid contact current, (f) lumped contact resistance, (g) self-consistently simulated V_d , (h) R_{grid} ; interruptions highlighted, (i) local grid voltage.

after (15) assuming a homogeneous grid resistance of $0.33 \Omega/\text{cm}$ (not shown here, but in Section 6.2) showed in the regions of isolated gridlines between two busbars bright lines, similar as the RESI- R_s image in Fig. 4(d) does, and in isolated grid regions the expected black-and-white horizontal stripes as discussed in Section 4.3. In these regions $R_{l,\text{contact}}$ cannot be measured accurately but has to be replaced by the average value of the surrounding for performing the self-consistent circuit evaluation after Section 5. Fig. 4(f) shows the such optimized image of $R_{l,\text{contact}}$ scaled in units of Ωcm^2 . Though this area-related resistance only acts below the gridlines, it is scaled here referred to the cell area for enabling a better comparison with RESI- R_s . We see that $R_{l,\text{contact}}$ is significantly smaller than RESI- R_s , since $R_{l,\text{contact}}$ does not contain the influence of the grid and emitter resistances.

Note that these data are relatively noisy, since the voltage drops across $R_{l,\text{contact}}$ are only in the low mV range, which is close to the accuracy limit of the EL measurement. As mentioned in the

Introduction and will be further discussed in Section 7, these data are significantly higher than the influence of typical grid contact resistances, since they contain also contributions from other inhomogeneities, e.g. from an inhomogeneous grid resistance. In particular in the upper part of the cell, this $R_{l,\text{contact}}$ image (f) appears in its average homogeneous between the busbars (compare to the RESI- R_s image d), which points to a sufficiently accurate choice of the homogeneous value of R_{grid} there. In the lower part of the cell a residual profile between the busbars remains, which points to higher values of R_{grid} there, as will be discussed in Section 7. In particular, in contrast to the RESI- R_s image (d), the $R_{l,\text{contact}}$ image (f) shows only minor local minima in the positions of local J_{01} maxima. If such minima exist (e.g. in the lower part of the cell), they are in regions of relatively large values of $R_{l,\text{contact}}$. Hence, in these regions R_{contact} is certainly overestimated, which will be further discussed in Section 7. This leads, similar as for RESI- R_s , in regions of J_{01} maxima to weak $R_{l,\text{contact}}$

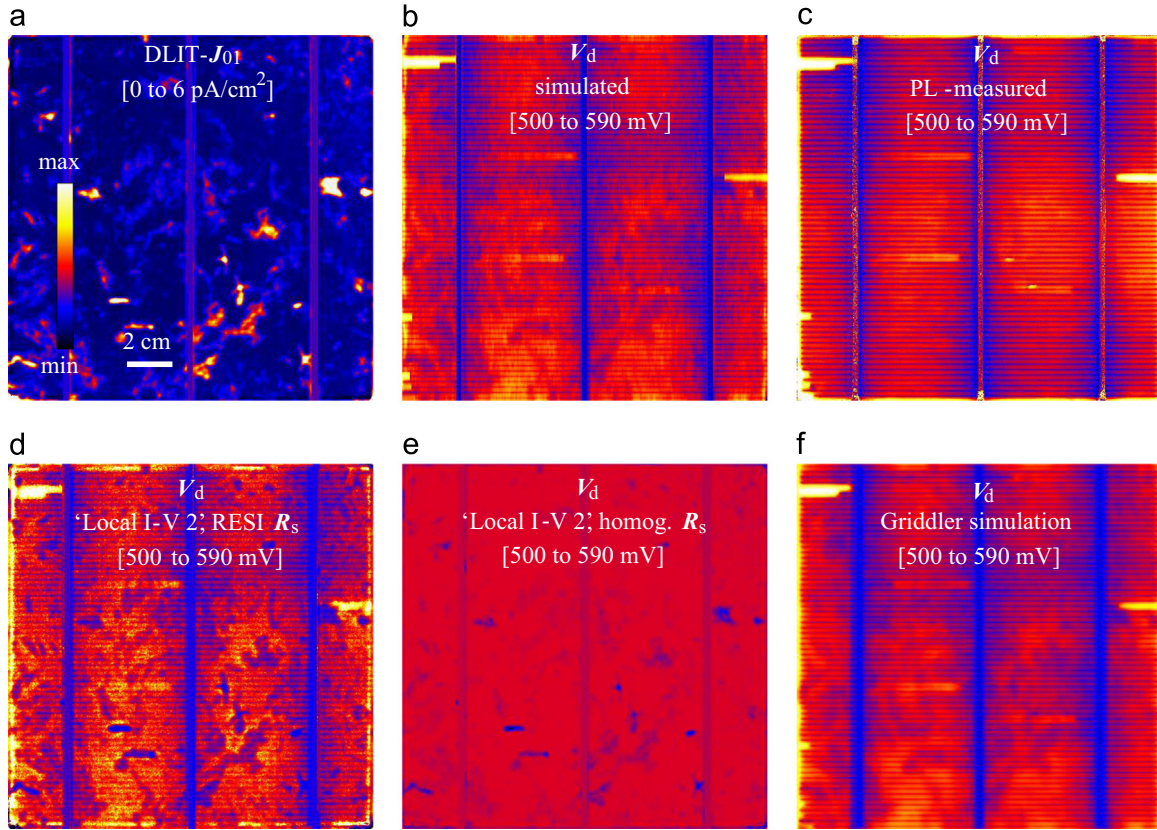


Fig. 5. (a) Effective J_{01} image after (2), (b) self-consistently simulated V_d at mpp, (c) PL-measured V_d at mpp, (d) V_d at mpp simulated in 'Local I-V 2', (e) V_d at mpp simulated using homogeneous R_s , and (f) V_d at mpp simulated for our R_s data by Griddler [2].

minima, which have to be considered as residual artifacts of our procedure.

The $R_{l,\text{contact}}$ image shown in Fig. 4(f) was used in the self-consistent calculation for $V=600$ mV in the dark. In this calculation the values of $R_{\text{grid},i}$ in the onset positions of all broken gridlines have been optimized by fitting the local V_d values as close as possible to the measured values of Fig. 4(a). Note that these resistances cannot have infinite values, since, even if the gridline should really be broken, this gap is bridged by the emitter. Our model of Fig. 3 does not contain any emitter conductivity parallel to the gridlines, therefore our grid resistance in breakage position remains finite, depending on the width of the gap, which has to be bridged by the emitter conductance. The self-consistently simulated local diode voltage image for the dark case is shown in Fig. 4(g), and (h) shows the resulting image of R_{grid} , which shows the broken gridlines as local maxima of different magnitude, see the fine vertical stripes. For pointing to these grid interruption positions, they are highlighted in (h) by dashed circles. Also the self-consistently simulated V_d data in Fig. 4(g) nicely coincide with Fig. 4(a) and (b), except that in (g) the voltage changes across broken gridlines appear much sharper. This difference is again due to the fact that our model in Fig. 3 does not consider the emitter conductivity parallel to the gridlines. Finally, Fig. 4(i) shows the distribution of the local grid voltage after (14). Note that the voltage drops shown in this image, as well as the local voltage profiles between neighboring gridlines, are attributed in all previously published R_s concepts to the effective R_s . In contrast, our concept divides the series resistance in a horizontal fraction, given by the emitter and the grid resistance, and the lumped contact resistance image shown in Fig. 4(f).

The decisive accuracy test of our concept is its application to the illuminated case, in particular to the mpp case where resistive effects play a role. The value of V_{mpp} of the cell used in this Section

was measured by a flasher (Sinton) to be 518 mV, the Local I-V analysis lead to $V_{\text{mpp}}=520$ mV. Here we have used the flasher value. Fig. 5(a) shows again the effective J_{01} image of this cell and (b) shows the local diode voltages simulated self-consistently under illumination at V_{mpp} . For comparison, (c) shows the local diode voltages measured by evaluating spatially deconvoluted PL images at J_{sc} and V_{mpp} as described in Section 2. We see a good correlation between (b) and (c). The additional noise in image (b) stems from the relatively noisy $R_{l,\text{contact}}$ image in Fig. 4(f). The ' J_{01} shunt' regions of locally increased J_{01} visible in (a) are hardly visible in the PL-based V_d image (c), but some of them (in the lower part of the cell) are weakly visible as local minima in Fig. 5(b). These differences will be further discussed in Section 7. For comparison, Fig. 5(d) shows the local diode voltages simulated under mpp condition by Local I-V 2 [20,21], which is based on the model of independent diodes and uses the RESI effective resistance concept [11]. In this image all J_{01} shunts show a strong local dip in the diode voltage. Fig. 5(e) shows the local diode voltage calculated in Local I-V 2 by assuming a homogeneous local resistance of $0.7 \Omega \text{ cm}^2$, which corresponds to the average of the RESI- R_s . Of course, this image does not show local diode voltage maxima between the busbars and gridlines and also not the broken gridline regions. However, it also shows local minima in regions of local J_{01} maxima, much stronger than in the 2D simulated image (b) but weaker than in the RESI-based image (d). Obviously there are two factors leading to the (wrong) local diode voltage minima in (d), first the R_s inhomogeneity assumed there in the RESI- R_s image and second the J_{01} inhomogeneity itself, which would act even for homogeneous effective R_s . The question is, why do we see this influence of J_{01} so weakly in the 'real' V_d image (c)? This question will be answered in Section 7.

Finally Fig. 5(f) shows the local diode voltages at mpp as simulated by Griddler [2]. For enabling the Griddler simulation, the

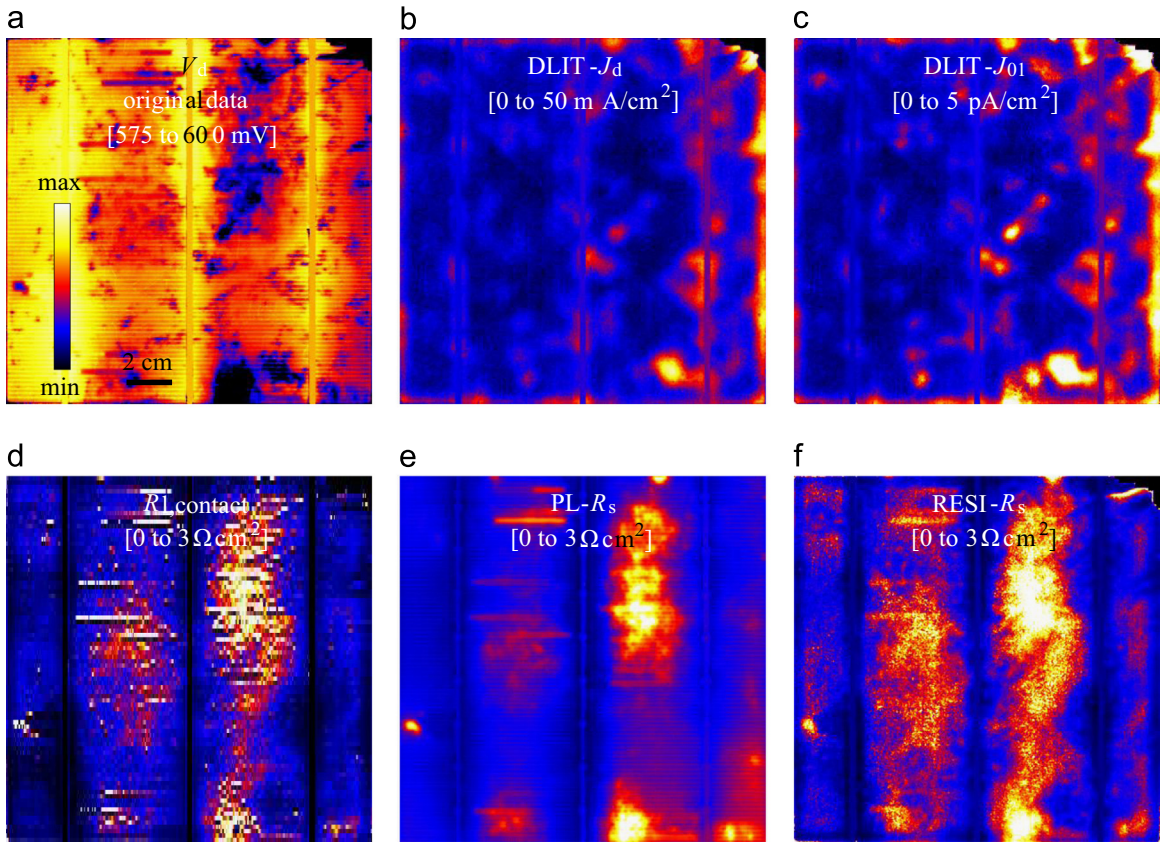


Fig. 6. (a) EL-measured V_d at 600 mV; data in grid positions extrapolated, (b) DLIT-measured J_d image at 600 mV, (c) effective J_{01} image after (2), (d) lumped contact resistance, grid interruptions not corrected, (e) PL- R_s image, (f) RESI- R_s image.

circuit parameters of our equivalent circuit were transferred into area-related parameters, which were used in a Griddler simulation of the cell performed at mpp. Griddler uses a much more sophisticated and realistic equivalent model for the solar cell with a higher number of knots, in particular it also considers emitter conductivity parallel to the gridlines. Nevertheless, the result in (f) is close to that in (b), which points to the applicability of the simplifications made in our calculation, in particular by neglecting the emitter conductivity parallel to the gridlines. Since this conductivity is regarded in the Griddler simulation, the V_d profile across the grid interruption sites is now again as smooth as it is in the PL-measured V_d image (c). This conductivity is also the reason why the noise in the Griddler image (f) is lower than that in image (b) of our simulation.

The difference between Fig. 5(b) and (d) is the major achievement of the method introduced here. The RESI- R_s image in Fig. 4(d) does perfectly describe the local diode voltage in the dark in Fig. 4(a), but not the illuminated case in Fig. 5. On the other hand, a PL-based R_s image (not shown here but in the next Section) would correctly describe the illuminated case but not the dark one. Only our R_s concept allows us to describe the local diode voltages reasonably both in the dark and under illumination by using the same set of local resistance data (R_{grid} and $R_{\text{l, contact}}$). Further improvements of the method are planned.

6.2. Cell with inhomogeneous R_{contact}

The cell used in this section was an experimental cell produced from multicrystalline material by the same technology as used for that in Section 6.1. For this cell the PL-measured R_s image indicated a locally increased contact resistance. Unfortunately, one corner of the cell was broken off, leading to some cracks in this area, but the cell still could be investigated. Fig. 6(a) shows

the EL-measured local voltage image after correcting the results for light scattering in the detector and extrapolating the data below the gridlines, as it was done for Fig. 4(a). Already this image shows indications of an increased series resistance in the inner fields of the cell, in particular in the field between the middle and the right busbar, whereas the field left of the left busbar shows a low series resistance. Fig. 6(b) shows an image of the DLIT-measured local diode current density J_d at the same bias of 600 mV. Fig. 6(c) shows an image of the effective J_{01} obtained after (2). This image is scaled that, in the low- R_s region left of the leftmost busbar, the brightness is the same as in the J_d image (b). Since the J_{01} image considers the reduced local voltages in the high- R_s regions, the brightness in the J_d image (b) in these regions is lower than in the J_{01} image (c). The procedure for calculating $R_{\text{l, contact}}$ described in Section 4 was applied to these data with the result shown in Fig. 6(d), again scaled referred to the cell area. Here the same values for the grid resistance ($0.33 \Omega/\text{cm}$) and the emitter resistance ($40 \Omega/\text{sq}$) as in the previous example were assumed, which lead to reasonable results. This cell contains many broken gridlines. In Fig. 6(d) the influence of broken gridlines was not corrected, which would have become complicated in the region of the missing corner and the cracks around. For comparison, the PL-measured R_s image and the RESI- R_s image are shown in Fig. 6(e) and (f). We see a very good correspondence between $R_{\text{l, contact}}$ (d) and PL- R_s (e). This proves again that, from all conventional R_s imaging methods, PL- R_s is most appropriate to display local inhomogeneities of R_s . The RESI- R_s image (f), on the other hand, which is based on the same Eq. (1) as PL- R_s , again shows the same regions of locally increased R_s , and in addition the expected artifacts (local minima) in the regions of J_{01} maxima. However, since in this example R_s is generally higher than in the last example and dominated by the

contact resistance, the visibility of these artifacts is lower than in Fig. 5(d). This shows that, if a cell shows real local R_s problems, they can be detected by all established R_s imaging techniques.

7. Discussion

It remains to explain why the local J_{01} maxima are not or only very weakly visible in the local diode voltage image under illumination at mpp, but in the dark they are, as shown in Fig. 5. This is again a consequence of the distributed character of R_s , hence of the fact that R_s in solar cells is governed by horizontal resistance components. Let us assume a local J_{01} shunt between two busbars, and let us assume that J_{01} in shunt position is just as large that, at mpp of the cell, the net current density in this position is zero. Then, in the dark, this shunt position is the position of highest dark current density, which expresses as a local minimum of the diode voltage, as expected. Due to the distributed (horizontal) nature of R_s this minimum is only laterally smeared, which has been called 'resistive blurring' in [13]. Under illumination at mpp, however, all regions around the shunt deliver their J_{mpp} , only the shunt position delivers zero net current. Then, in regions without the shunt, we expect a parabolic local diode voltage profile between the busbars, since the second derivative of the local voltage is proportional to the diode current density. If there is a shunt, the shunt region would only show zero second derivative, but all other regions contribute as before. Hence, in this position the two parabolic branches left and right of the shunt are just connected by a straight line. Thus, if the shunt region is small enough, this shunt would hardly influence the local voltage profile under illumination, but in the dark it clearly does. Again, the final reason for this different behavior is the different diode current density profile in both cases, which is very inhomogeneous in the dark but, in most parts of the cell, homogeneous in the illuminated case.

This is the first estimate to fit measured image data of real inhomogeneous solar cells to the components of an equivalent circuit of the cell. This estimate is far from being perfect yet. In particular, the lumped contact resistance values obtained by us are still significantly higher than realistic contact resistances. We see at least two or several reasons for this. First, our evaluation points to an emitter sheet resistance of 40 Ω/sq , but in reality we expect about 50 Ω/sq or even more. When we fitted our model to local diode voltage data obtained from non-deconvoluted EL data, this could be explained only by an emitter sheet resistance of only 20 Ω/sq . Since our emitter resistance is still slightly too low, we believe that there is another blurring effect influencing the EL images, besides photon scattering in the detector. This may be e.g. carrier smearing in the bulk, as has been reported by Phang et al. [36]. Unfortunately, the method proposed there for solving this problem only works on wafers, but not on cells. Assuming a higher emitter resistance in our simulations would lead to lower $R_{l, \text{contact}}$ values. Moreover, we have assumed a homogeneous value of R_{grid} , except in the positions of grid interruptions. Our obtained $R_{l, \text{contact}}$ data in Fig. 4(f) show a clear tendency to increase towards the bottom of the cell. This may be an indication that the grid resistance increases towards the bottom, e.g. by varying the grid thickness. Such an inhomogeneity can easily appear in the screen-printing process used for fabricating the grid. In our simulations we could not further increase the assumed value of R_{grid} , since then in the upper part of the cell negative values of $R_{l, \text{contact}}$ would appear. If, however, higher values of R_{grid} would be assumed only in the lower part of the cell, significantly lower values of $R_{l, \text{contact}}$ would appear there. Then it could be expected that $R_{l, \text{contact}}$ would become independent from J_{01} everywhere, as it is actually expected, and the self-consistent simulation of the illuminated

mpp case would be even more realistic. An alternative approach to that used in this work would be to assume a homogeneous R_{contact} and to consider R_{grid} as a local variable. However, this approach would not allow us to analyze cells with really inhomogeneous contact resistance, as we did in Section 6.2. Thus, the method introduced here should certainly be further improved.

8. Conclusions

In this contribution a concept for describing the local series resistance of real solar cells is introduced, which is based on a two-dimensional equivalent circuit simulation. A strategy is proposed to fit the components of this circuit to results of EL and DLIT imaging of the investigated cell. Our model uses separate resistances for horizontal and vertical current flow, thereby explicitly considering the distributed nature of the series resistance. Here the vertical diode, emitter, and grid resistances are assumed to be homogeneous (except R_{grid} in positions of grid interruptions), and J_{01} and the 'lumped grid contact resistance' are taken as local variables. The remaining limitations of this simple concept are shown and ways to overcome them are discussed. Nevertheless this concept allows for the first time to describe the local voltage drops in an inhomogeneous solar cell reasonably both in the dark and under illumination, based on imaging results.

Acknowledgments

The authors are grateful to Johnson Wong (SERIS Institute, Singapore) for performing the Griddler simulations, to A. van der Heide (Soltech, Tienen, Belgium) and to Hannes Höffler (Fraunhofer ISE, Freiburg) for providing cells for these investigations and the PL- R_s image in Fig. 6(e), and to Jan Bauer (MPI Halle) and J.-M. Wagner (Kiel University, Germany) for valuable discussions. The authors acknowledge the financial support by the German Federal Ministry for Commerce and Energy and by industry partners within the research cluster "SolarLIFE" (contract No. 0325763 D). The content is in the responsibility of the authors.

References

- [1] K. Bothe, D. Hinken, Quantitative luminescence characterization of crystalline silicon solar cells, in: G.P. Willeke, E.R. Weber (Eds.), *Advances in Photovoltaics*, vol. 2, Academic Press (Burlington), Elsevier, 2013.
- [2] J. Wong, Griddler: Intelligent computer aided design of complex solar cells, in: Proceedings of the 40th IEEE PVSC, Tampa, 2013, pp. 933–938.
- [3] A.S.H. van der Heide, J.H. Bultman, J. Hoornstra, A. Schönecker, Error diagnosis and optimisation of c-Si solar cell processing using contact resistances determined with the Corescanner, *Sol. Energy Mater. Sol. Cells* 74 (2002) 43–50.
- [4] P.E. Mijnarends, G.J.M. Janssen, W.C. Sinke, The effect of material inhomogeneities on the characteristics of semicrystalline silicon solar cells: the second diode, *Sol. Energy Mat. Sol. Cells* 33 (1994) 345–360.
- [5] T. Trupke, E. Pink, R.A. Bardos, M.D. Abbott, Spatially resolved series resistance of silicon solar cells obtained from luminescence imaging, *Appl. Phys. Lett.* 90 (2007) 093506.
- [6] J. Haunschild, M. Glatthaar, M. Kasemann, S. Rein, E.R. Weber, Fast series resistance imaging for silicon solar cells using electroluminescence, *Phys. Stat. Sol. RRL* 3 (2009) 227–229.
- [7] M. Glatthaar, J. Haunschild, M. Kasemann, J. Giesecke, W. Warta, St. Rein, Spatially resolved determination of dark saturation current and series resistance of silicon solar cells, *Phys. Status Solidi RRL* 4 (2010) 13–15.
- [8] M. Glatthaar, J. Haunschild, R. Zeidler, M. Demant, J. Greulich, B. Michel, W. Warta, R. Preu, Evaluating luminescence based voltage images of solar cells, *J. Appl. Phys.* 108 (2010) 014501.
- [9] H. Kampwerth, T. Trupke, J.W. Weber, Y. Augarten, Advanced luminescence based effective series resistance imaging of silicon solar cells, *Appl. Phys. Lett.* 93 (2008) 202102.
- [10] C. Shen, H. Kampwerth, M. Green, T. Trupke, J. Carstensen, A. Schütt, Spatially resolved photoluminescence imaging of essential silicon solar cell parameters

- and comparison with CELLO measurements, *Sol. Energy Mat. Sol. Cells* 109 (2013) 77–81.
- [11] K. Ramspeck, K. Bothe, D. Hinken, B. Fisher, J. Schmidt, R. Brendel, Recombination current and series resistance imaging of solar cells by combined luminescence and lock-in thermography, *Appl. Phys. Lett.* 90 (2007) 153502.
- [12] O. Breitenstein, J. Bauer, K. Bothe, D. Hinken, J. Müller, W. Kwapił, M.C. Schubert, W. Warta, Can luminescence imaging replace lock-in thermography on solar cells? *IEEE J. Photovolt.* 1 (2011) 159–167.
- [13] O. Breitenstein, J. Bauer, D. Hinken, K. Bothe, The reliability of thermography- and luminescence-based series resistance and saturation current density imaging, *Sol. Energy Mater. Sol. Cells* 137 (2015) 50–60.
- [14] G. Araujo, A. Cuevas, J.M. Ruiz, The effect of distributed series resistance on the dark and illuminated current–voltage characteristics of solar cells, *IEEE Trans. Electron Devices* 33 (1986) 391–401.
- [15] O. Breitenstein, S. Rißland, A two-diode model regarding the distributed series resistance, *Sol. Energy Mat. Sol. Cells* 110 (2013) 77–86.
- [16] J. Carstensen, J.-M. Wagner, A. Schütt, A. Krudopp, H. Föll, Ohmic loss analysis for lateral balancing currents by CELLO and photoluminescence measurements, in: Proceedings of the 29th EU Photovoltaic Solar Energy Conference, Amsterdam 2014, pp. 433–440.
- [17] J. Carstensen, J.-M. Wagner, A. Schütt, R. Adelung, Solving the code of series resistance on large area solar cells: Average and local power losses of external and lateral balancing currents, in: Proceedings of the 31st EU Photovoltaic Solar Energy Conference, Hamburg, 2015, pp. 838–844.
- [18] J.-M. Wagner, M. Hoppe, A. Schütt, J. Carstensen, H. Föll, Injection-level dependent series resistance: Comparison of CELLO and photoluminescence-based measurements, *Energy Procedia* 38 (2013) 199–208.
- [19] D. Walter, A. Liu, E. Franklin, D. Macdonald, B. Mitchell, Th. Trupke, Contrast enhancement of luminescence images via point-spread deconvolution, in: Proceedings of the 38th IEEE PVSC, Austin, TX, 2012, pp. 307–312.
- [20] O. Breitenstein, Nondestructive local analysis of current–voltage characteristics of solar cells by lock-in thermography, *Sol. Energy Mat. Sol. Cells* 95 (2011) 2933–2936.
- [21] O. Breitenstein, Local efficiency analysis of solar cells based on lock-in thermography, *Sol. Energy Mat. Sol. Cells* 107 (2012) 381–389.
- [22] T. Fuyuki, A. Kitayanan, Photographic diagnosis of crystalline silicon solar cells utilizing electroluminescence, *Appl. Phys. A* 96 (2009) 189–196.
- [23] M.A. Green, M.J. Keevers, Optical properties of intrinsic silicon at 300 K, *Prog. Photovolt. Res. Appl.* 3 (1995) 189–192.
- [24] Data sheet of ANDOR iKon-M PV Inspector camera, (<http://www.andor.com/scientific-cameras/ikon-ccd-camera-series/pv-inspector>) (January 2016).
- [25] A. Teal, M. Juhl, Correcting the inherent distortion in luminescence images of silicon solar cells, in: Proceedings of the 42nd IEEE Photovoltaic Specialists Conference, New Orleans, 2015, <http://dx.doi.org/10.1109/PVSC.2015.7356303>.
- [26] O. Breitenstein, F. Fröhlauf, A. Teal, An improved method to measure the point spread function of cameras used for electro- and photoluminescence imaging of silicon solar cells, *IEEE J. Photovolt.* 6 (2016) 522–527.
- [27] M. Köntges, M. Siebert, D. Hinken, U. Eitner, K. Bothe, T. Potthof, Quantitative analysis of PV-modules by electroluminescence images for quality control, in: Proceedings of the 24th EU Photovoltaic Solar Energy Conference, Hamburg, 2009, pp. 3226–3231.
- [28] O. Breitenstein, A. Khanna, Y. Augarten, J. Bauer, J.-M. Wagner, K. Iwig, Quantitative evaluation of electroluminescence images of solar cells, *Phys. Stat. Solidi RRL* 4 (2010) 7–9.
- [29] see www.maxplanckinnovation.de/en (January 2016).
- [30] D. Macdonald, A. Cuevas, Reduced fill factors in multicrystalline silicon solar cells due to injection-level dependent bulk recombination lifetimes, *Prog. Photovolt.: Res. Appl.* 8 (2000) 363–375.
- [31] S. Rißland, O. Breitenstein, Evaluation of luminescence images of solar cells for injection-level dependent lifetimes, *Sol. Energy Mater. Sol. Cells* 111 (2013) 112–114.
- [32] O. Breitenstein, Understanding the current–voltage characteristics of industrial crystalline silicon solar cells by considering inhomogeneous current distributions, *Opto-Electron. Rev.* 21 (2013) 259–282.
- [33] O. Breitenstein, W. Warta, M. Langenkamp, Lock-in thermography – basics and use for evaluating electronic devices and materials, second edition, Series in Advanced Microelectronics, vol. 10, Springer, Heidelberg, 2010.
- [34] O. Breitenstein, F. Fertig, J. Bauer, An empirical method for imaging the short circuit current density in solar cells based on dark lock-in thermography, *Sol. Energy Mat. Sol. Cells* 143 (2015) 406–410.
- [35] see <http://de.mathworks.com/products/matlab/index.html?requestedDomain=uk.mathworks.com> (January 2016).
- [36] S.P. Phang, H.C. Sio, D. Macdonald, Carrier de-smearing of photoluminescence images on silicon wafers using the continuity equation, *Appl. Phys. Lett.* 103 (2013) 192112.